

Journal of Materials Chemistry A

Accepted Manuscript



This is an *Accepted Manuscript*, which has been through the Royal Society of Chemistry peer review process and has been accepted for publication.

Accepted Manuscripts are published online shortly after acceptance, before technical editing, formatting and proof reading. Using this free service, authors can make their results available to the community, in citable form, before we publish the edited article. We will replace this *Accepted Manuscript* with the edited and formatted *Advance Article* as soon as it is available.

You can find more information about *Accepted Manuscripts* in the [Information for Authors](#).

Please note that technical editing may introduce minor changes to the text and/or graphics, which may alter content. The journal's standard [Terms & Conditions](#) and the [Ethical guidelines](#) still apply. In no event shall the Royal Society of Chemistry be held responsible for any errors or omissions in this *Accepted Manuscript* or any consequences arising from the use of any information it contains.

Cite this: DOI: 10.1039/c0xx00000x

www.rsc.org/xxxxxx

In situ spectroscopy studies of CO₂ adsorption in a dually functionalized microporous metal-organic framework

Yuan Chen,^a Hao Wang,^b Jing Li,^b and Jenny V. Lockard^{*a}

Received (in XXX, XXX) Xth XXXXXXXXX 20XX, Accepted Xth XXXXXXXXX 20XX

DOI: 10.1039/b000000x

The activation and CO₂ gas adsorption processes in the *rht*-type metal-organic framework, [Cu₃(TDPAT)(H₂O)₃]·10H₂O·5DMA (TDPAT=2,4,6-tris(3,5-dicarboxylphenylamino)-1,3,5-triazine) were investigated on the molecular level using several spectroscopic characterization methods. The remarkable selectivity of this framework for CO₂ is attributed to the high density of coordinatively unsaturated metal nodes and amine linker functionality that both serve as gas binding sites. Spectroscopic evidence for these binding interactions as well as the concomitant electronic and molecular level structure changes of the host framework and CO₂ guest is derived from a combination of *in situ* UV-vis diffuse reflectance, X-ray absorption and Raman spectroscopy studies. Results showed that the activation process produced subtle structural rearrangements of the framework that may be influencing the binding interactions upon subsequent CO₂ adsorption.

Introduction

Metal organic frameworks (MOFs) are an emerging class of hybrid materials composed of metal ions or clusters connected by organic molecules to form crystalline microporous architectures. The tunable chemical composition, pore size and shape and the unique functionalities these attributes afford make MOF materials ideal for potential adsorption-based applications such as gas separation and storage, heterogeneous catalysis, luminescence-based sensing and others. Several recent reviews have highlighted the progress made in developing MOFs for these applications.¹⁻⁹ Current interest in carbon sequestration technology for reducing the amount of atmospheric greenhouse gases has prompted the development of MOF materials for selective CO₂ filtering to prevent its release into the atmosphere, for example from the flue gas emissions of industrial processes. In contrast to conventional CO₂ adsorption technologies, which often suffer from either low capacity or low selectivity, MOFs can be designed with high densities of potential binding sites with strong affinities for CO₂ molecules. For example, the well-studied framework, MOF-74¹⁰ (also known as CPO-27)^{11, 12} exhibits exceptional CO₂ uptake and selectivity, particularly for the Mg version, due to its large surface to volume ratio and the favorable binding between CO₂ and the accessible open metal sites lining the channels of the framework.^{13, 14} Other frameworks take advantage of the Lewis basicity of amines for promoting CO₂ adsorption ability by incorporating them at linker positions.^{15, 16} Furthermore, a handful of frameworks incorporate both types of binding sites (i.e. coordinatively unsaturated metal nodes and amine functionalized linkers) as a strategy for improving MOF CO₂

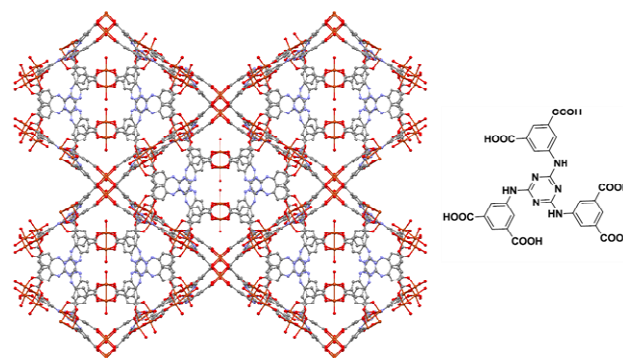


Fig. 1 Crystal structure of **1** (left) and H₆TDPAT linker (right) adsorption performance.^{17, 18} In all these frameworks, an in-depth understanding of the intrinsic host-guest interactions behind the CO₂ adsorption mechanism, which has been the target of several recent experimental and computational studies,¹⁹⁻²³ will be helpful in directing the design of new MOFs for this adsorption-based application. The added structural complexity of dually functionalized frameworks makes assessing the adsorption mechanism especially complicated and a task best tackled using multiple *in situ* characterization methods.

In this paper we focus on the Cu-based MOF depicted in Figure 1, [Cu₃(TDPAT)(H₂O)₃]·10H₂O·5DMA (TDPAT=2,4,6-tris(3,5-dicarboxylphenylamino)-1,3,5-triazine), also known as *rht*-MOF-7, hereafter denoted **1**. This MOF, which has previously been reported,^{24, 25} was designed to have both types of potential binding sites for CO₂ adsorption described above; coordinatively

unsaturated metals and secondary amine linker functionality. As in other *rht*-type MOFs²⁶⁻³² with potentially open metal sites, the paddle wheel Cu sites in **1** are rendered pore wall accessible by removal of coordinated labile solvent molecules through thermal activation. The secondary amines that serve as Lewis base sites for gas adsorption are incorporated on the phenyl groups of the triazine linkers. While its remarkable selectivity for CO₂ adsorption has been shown by gas isotherm measurements^{24, 25} and further substantiated through computational studies,^{22, 23} the specific molecular level interactions and framework structure changes associated with that behavior have not been evaluated in great detail. In this work, the activation and CO₂ gas adsorption processes in **1** are probed using a combination of *in situ* spectroscopy techniques, namely UV-visible diffuse reflectance, X-ray absorption and Raman spectroscopy. While the diffuse reflectance measurements probe valence electron transitions, XAS involves monitoring specific core electron transfer processes. Both methods are well suited for studying metal containing materials. The former provides valuable electronic and indirect geometry information through the behavior of the d-d absorption bands. The interpretation of both the X-ray absorption near edge structure (XANES) and extended X-ray absorption fine structure (EXAFS) spectral regions allows complementary evaluation of metal oxidation state, coordination geometry and short range distance information. XAS is well established in the study of other solid state porous materials such as zeolites³³⁻³⁷ and while it is increasingly being incorporated in the arsenal of MOF characterization methods, its utility has been primarily limited to aiding the refinement of MOF crystal structures and verifying the coordination environments of post-synthetically incorporated metal sites.³⁸⁻⁴⁰ When applied to MOF materials through *in situ* measurement, this technique can provide electronic and atomic level distance information needed to determine potentially important metal electron distribution and framework structural changes during the host-guest adsorption events. In addition to our own work,⁴¹ other studies have employed XAS to interrogate the local metal coordination in MOF materials upon activation and subsequent adsorption of various gases.^{40, 42, 43} Raman spectroscopy is another important characterization technique amenable to both *in situ* and solid state sample measurement. In the context of this work, it is used to monitor the vibrational frequencies assigned to the different components of the framework and the adsorbed CO₂ molecules within the pores. The important structural changes and relative participation of the different framework components are implicated by the observed changes in the individual Raman modes. The utility of this technique has been demonstrated for the structural characterization of MOF materials and their adsorption processes.^{19, 41, 44-53} Each technique has its limitations, but when combined, they generate a more complete picture of activation and gas adsorption process and the local structural ramifications.

Experimental Section

MOF Materials.

1 was synthesized following the previously published procedure,²⁴ and all samples were characterized by powder X-ray diffraction to verify the crystallinity. (see Supporting Information

for additional details on synthesis and PXRD measurements).

Diffuse reflectance spectroscopy.

Diffuse reflectance spectra of **1** were collected using a Cary-Varian UV-visible-NIR spectrophotometer equipped with a diffuse reflectance accessory and controlled environment (vacuum/gas and temperature) solid state sample holder (Harrick Instruments). Adsorption spectra of the sample mixed with KBr were collected at 10 °C intervals from 30 °C to 120 °C under dynamic vacuum. After cooling the sample to room temperature adsorption data were collected upon subsequent purging with CO₂ gas until no further spectral changes were observed.

X-ray Characterization.

X-ray absorption data were collected at the copper K-edge (8979eV) in transmission mode at Beamline X18A at the National Synchrotron Light Source (NSLS). The X-ray white beam was monochromatized by a Si(111) monochromator and detuned by 25% to minimize the harmonic content of the beam. Copper foil was used as the reference for energy calibration. The incident beam intensity (I_0) was measured by a 15 cm ionization chamber with 100% N₂. The transmitted beam intensity (I_t) and reference (I_r) were both measured by a 30 cm ionization chamber with 60% N₂ and 40% Ar. XAS spectra were collected during heat activation, CO₂ adsorption and H₂O re-coordination using a Claussen cell reactor. This cell, which has previously been described,⁵⁴ enables simultaneous controlled temperature and gas flow environment on a sample contained within a 3mm diameter Kapton tube for *in situ* measurements. A mixture of 5 mg of **1** thoroughly ground with ~100 mg of boron nitride was packed into the sample tube to yield approximately one X-ray absorption length. Three XAS spectra of the as-synthesized sample were first collected at room temperature (~25 °C) under continuous He gas purge. Spectra were continuously collected during heat activation of the sample (ie. gradual heating to 150 °C under He gas flow) until no further spectral changes were observed to ensure complete dehydration. Another three scans were collected once the sample was cooled back to 25°C to void the temperature effects on the Debye-Waller factor in comparison between hydrated and dehydrated sample data. The sample was then purged with dry CO₂ while continuously collecting XAS data to monitor the uptake of CO₂ in the framework. Finally, *in situ* XAS was used to monitor the MOF rehydration process. In this step, the same sample, having undergone the treatments described above, was first thermally reactivated and then cooled to room temperature under dry He flow to drive off adsorbed CO₂. The reactivated sample was then purged with “wet” helium gas (i.e. He was sent through a bubbler containing water prior to exposure to the MOF sample) to recover the hydrated framework. XAS spectra were collected throughout this process to monitor the rehydration structure. All XAFS data were processed and analyzed using the Athena and Artemis programs of the IFEFFIT package based on FEFF 6.^{55, 56}

The crystallinity of this MOF sample was monitored by synchrotron PXRD (Figure S1) immediately before and after each adsorption/desorption step described above to show that the crystallinity and long range order were preserved throughout the process.

Results

UV-vis diffuse reflectance spectroscopy

The diffuse reflectance spectra of **1** obtained during activation and CO₂ gas treatment are shown in Figure 2. Spectral shift of the lowest energy band is observed almost immediately upon heating and no further change occurs after 70 °C. The maximum absorption of the lowest energy band is observed to blue shift from 708 to 581 nm upon dehydration. Upon subsequent exposure to CO₂ gas environment, the absorption maximum red shifts to a final peak position of 608 nm.

X-Ray Absorption Spectroscopy

Averages of three XAS scans obtained at room temperature, including before and after activation, as well as after CO₂ loading and rehydration are depicted in Figures 3 and 4. The changes occurring in the XANES region under these conditions are shown in Figure 3 while the EXAFS data and corresponding fits of the CO₂-loaded and rehydrated sample are presented in Figure 4. In the latter, EXAFS spectra are shown as the Fourier transform $\chi(R)$ spectra produced using a k range of 2-12.5 Å⁻¹ and k weight of 2. The calculated fit to these data was performed over an R range 1.0-3.1 Å and was generated using a model based on the theoretical scattering paths derived from the reported single crystal data of **1**.²⁴ The parameter values obtained from the best fits are summarized in Table 1. For the hydrated material, the EXAFS fit was generated using fixed scattering path degeneracies, N , as determined by the single crystal structure model while the amplitude term, S_0^2 , the energy shift, ΔE_0 , effective length of the scattering path R_{eff} , and mean-square disorder term of neighbor atoms σ^2 for each of these paths were variable parameters. The same model without the Cu-O_{water} scattering path was used to fit the post-activation EXAFS data. In this case, the S_0^2 and ΔE_0 values were fixed to those obtained from the pre-activation fit along with the remaining scattering path degeneracies. The scattering path effective distance and disorder parameters however were used as variables. Finally, to fit the spectrum of the CO₂-loaded material the fitting model included an axially positioned O to generate the relevant Cu-O_{CO2} scattering path. It should be noted that EXAFS has limited utility for distinguishing among scattering paths involving the same or similar atoms, such as C, N or O. The fitting scheme described above is only possible because of the ability to restrict the fitting model using *a priori* knowledge of the exact coordination environment from single crystal data and the overall change in coordination known to occur upon the activation and gas adsorption. Nevertheless, some ill-defined fitting parameters are inevitable since the structure predicts several overlapping scattering paths that contribute to the same region of the EXAFS spectrum beyond the first shell peak. An analysis of these data and fits in the context of providing specific structural details about the dehydrated metal sites and their CO₂ interactions, including their limitations, is described in the Discussion Section.

Raman spectroscopy

Raman spectra collected upon activation and gas adsorption of **1** are shown in Figure 5. The observed vibrational frequencies along with corresponding mode assignments are summarized in

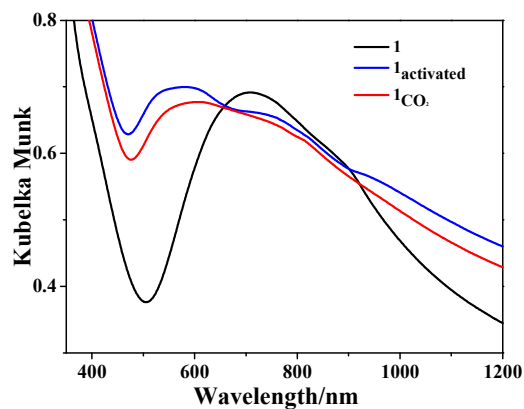


Fig. 2 In-situ absorption spectroscopy of **1** (black), activated **1** (blue), activated **1** treated with CO₂ (red).

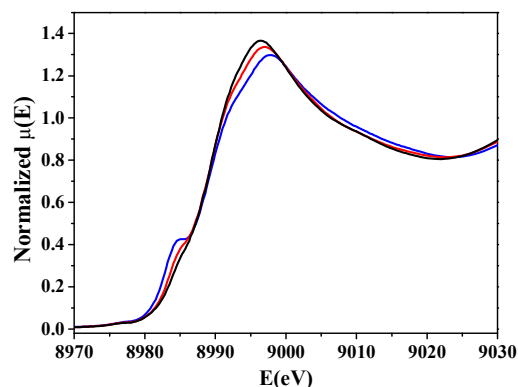


Fig. 3 Copper K-edge XANES spectra of **1** (black), activated **1** (blue), activated **1** treated with CO₂ (red) all obtained at room temperature.

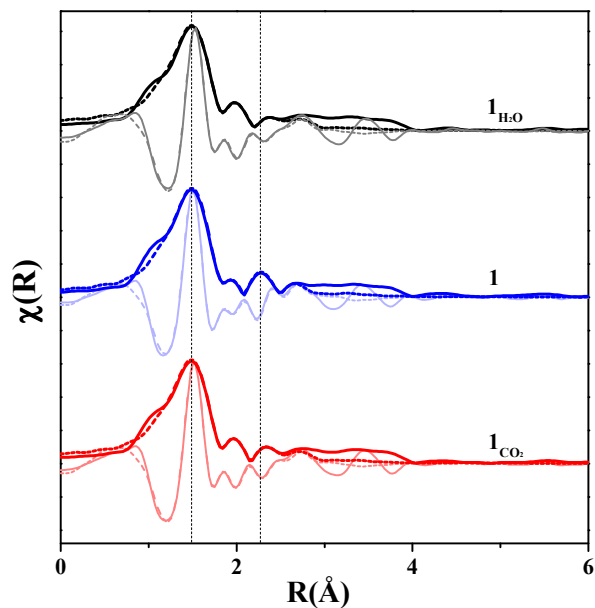


Fig. 4 Comparison between experimental EXAFS data (solid line) with theoretical fit (dashed line) in R -space, both magnitude (thick lines) and real (thin lines) components shown.

Table 1 Summary of EXAFS fitting Parameters

Scattering Path	degeneracy (N)	$R_{\text{eff}}(\text{\AA})$	$\sigma^2(\text{\AA}^2)$
I_{Hydrated} : $R^2=0.002$			
Cu _{abs} -O1	4	1.96 ± 0.01 (1.94) ^b	0.005 ± 0.001
Cu _{abs} -O _{water}	1	2.11 ± 0.08 (2.13)	0.018 ± 0.024
Cu _{abs} -Cu2	1	2.65 ± 0.04 (2.63)	0.008 ± 0.004
Cu _{abs} -C	4	2.87 ± 0.05 (2.84)	0.005 ± 0.005
Cu _{abs} -C-O	8	3.00 ± 0.06 (3.02)	0.006 ± 0.008
$I_{\text{Activated}}$: $R^2=0.003$			
Cu _{abs} -O1	4	1.94 ± 0.004	0.005 ± 0.001
Cu _{abs} -Cu2	1	2.55 ± 0.04	0.011 ± 0.004
Cu _{abs} -C	4	2.83 ± 0.03	0.006 ± 0.004
Cu _{abs} -C-O	8	2.96 ± 0.04	0.004 ± 0.005
I_{CO_2} : $R^2=0.003$			
Cu _{abs} -O1	4	1.95 ± 0.01	0.005 ± 0.001
Cu _{abs} -Oco ₂	0.76 ± 0.5^a	2.14 ± 0.13	0.017 ± 0.034
Cu _{abs} -Cu2	1	2.63 ± 0.06	0.009 ± 0.006
Cu _{abs} -C	4	2.86 ± 0.06	0.005 ± 0.005
Cu _{abs} -C-O	8	2.99 ± 0.06	0.006 ± 0.008

$\Delta E_0=3.8\text{eV}$, $S_0^2=1.02$, ^a variable parameter; ^b values in parenthesis obtained from crystal structure.

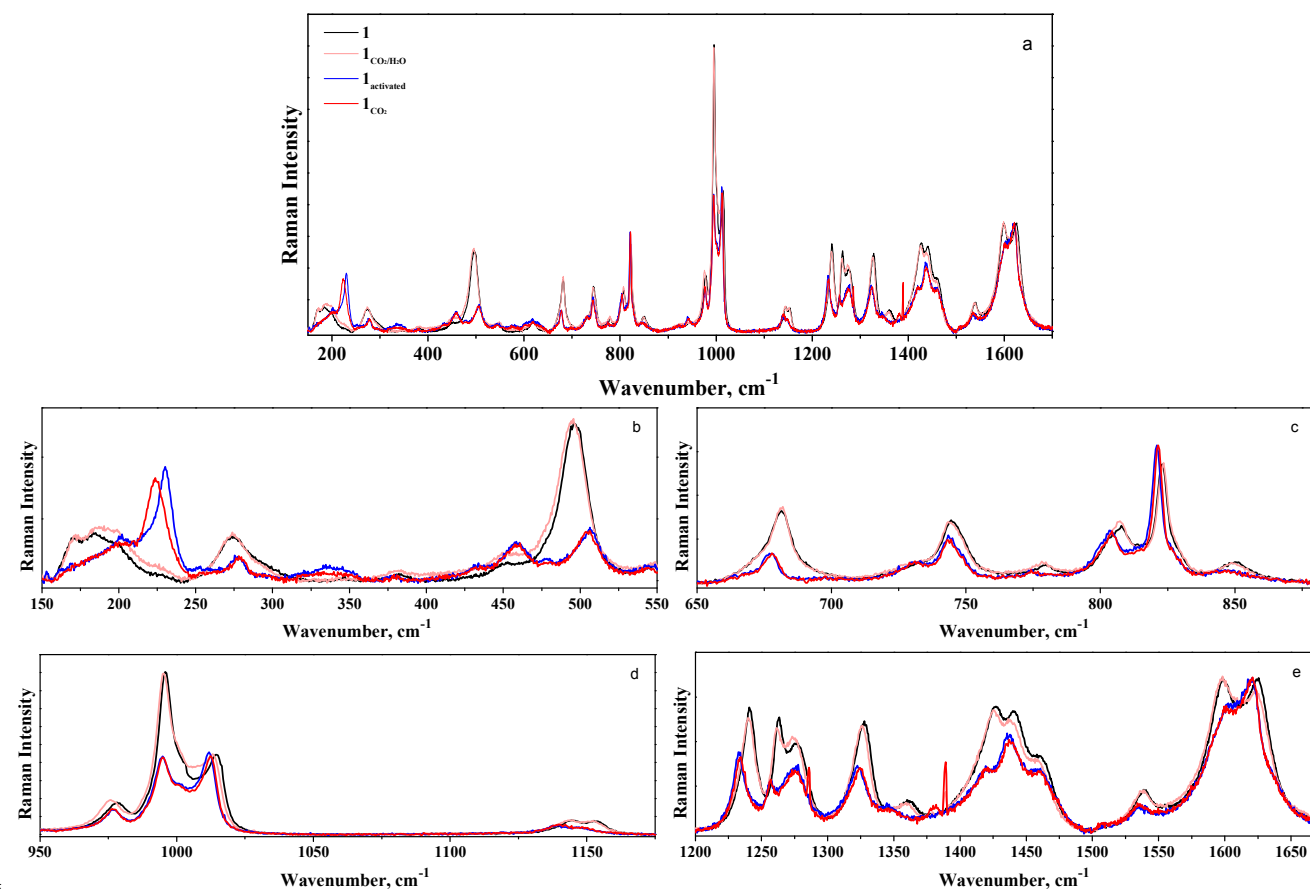


Fig.5 Full spectra of as-synthesized **1** (black), **1** treated with H₂O saturated CO₂ (pink), activated **1** (blue), activated **1** treated with pure CO₂ gas (red); (b-e) expanded spectral regions of the Raman full spectra in (a).

Table 2. Experimental Raman Frequencies and Corresponding Vibrational Mode Assignments of **1**

l	l _{CO₂/H₂O}	l _{activated}	l _{CO₂}	Raman assignment
171	171	sh	sh	v(Cu-Cu) + others
-	-	230	223	v(Cu-Cu)
274	274	278	278	Phenyl ring tilt
-	-	459	459	v(Cu-O) + γ(CH)
497	496	-	-	
-	-	506	505	δ Triazine ring
681	681	677	677	
744	744	743	743	δ Phenyl ring + γ(CH) β(OCO) _{carboxylate}
808	807	803	804	
823	823	821	822	
978	976	977	977	Triazine ring breathing mode
996	995	995	995	Phenyl ring breathing mode
1015	1013	1012	1012	v Triazine ring
1145	1145	1139	1140	β(CH)
1153	1152	sh	sh	β(CH)
1241	1240	1232	1234	v(CN) _{triazine} + ω(NH)
1263	1262	1257	1257	v(CN) + ω(NH) + ω(CH)
1277	1274	1275	1275	v(CN)
-	1286	-	1286	v(CO ₂)
1328	1326	1323	1325	v(CC) _{ph} + v(CN)
-	-	-	1381	v(CO ₂) _{coordinated}
-	1389	-	1389	v ₊ (CO ₂)
1427	1425	1420	1420	v _{sym} (COO ⁻)
1441	1436	1437	1437	ω(CH)+ω(NH)
1539	1539	1535	1534	v _{asym} (COO ⁻)
1598	1597	1603	1601	v(CC) _{ph}
1625	1624	1621	1621	v(CN)

v, stretching; β, in-plane-bending; γ, out-of-plane bending; ω, in plane wag; δ, deformation; sh, shoulder

Table 2. Vibrational mode assignments were made by comparison with well-established literature values,⁵⁷⁻⁶¹ the H₆TDPAT ligand spectrum and its computed theoretical vibrational mode frequencies. These reference spectra can be found in the Supplemental Information section (Figure S2) along with a summary of the DFT calculated H₆TDPAT vibrations in Table S1. Accordingly, the intense overlapping peaks at 1598 and 1625 cm⁻¹ are assigned to the phenyl C-C and amine C-N stretching modes respectively. The peaks in the 1200-1500 cm⁻¹ region are dominated by C-C stretch, C-N stretch as well as C-H and N-H wagging modes of the linker. The main peak at 996 cm⁻¹ is assigned to a phenyl ring breathing mode while the peak at 978 cm⁻¹ is assigned to a triazine ring breathing mode. The region of the spectrum below ~900 cm⁻¹ contains the low energy distortion modes of the linker and also those involving the metal site distortions. A triazine ring distortion mode occurs at 681 cm⁻¹ in the hydrated framework and downshifts to 677 cm⁻¹ upon activation. The strong feature at 497 cm⁻¹ is assigned to a Cu-O stretch that includes coordinated water oxygen since it is not present in the ligand Raman spectrum and drastically changes upon activation. The peak in this region observed at 506 cm⁻¹ for the activated framework is also attributed to this Cu-O stretch involving only the remaining metal carboxylate oxygen bonds.

The broad peak at 171 cm⁻¹ in the hydrated framework most likely contains a number of overlapping modes including modes involving the weakly interacting Cu sites spanning the paddlewheel node. A Cu-Cu stretching vibration is more evident in the activated framework spectrum which contains a well-resolved upshifted peak at 230 cm⁻¹ and is consistent with the vibrational assignments of other Raman studies on similar Cu frameworks.⁶²

Discussion

1. Local metal coordination changes upon activation and CO₂ gas adsorption.

The single crystal structure of **1** in its as-synthesized form (Figure 1) shows that the Cu sites have a distorted square pyramidal symmetry, excluding the weak Cu-Cu interactions spanning the paddlewheel node. Simple ligand field theory can be used to rationalize this geometry and predict the trend in geometry change upon dehydration and CO₂ interaction. In the hydrated coordination environment, the electrostatic repulsion from coordinated water molecule drives the carboxylate oxygens out of plane from the Cu(II) ions, while removal of these z-axis ligated molecules (through activation) eliminates this repulsion, predicting a structure change toward square planar. The electronic ramifications of this altered coordination geometry lead to a larger d-orbital energy level splitting through energy stabilization of the z-component *d*-orbitals and destabilization of the x,y-plane *d*-orbitals. Upon axial binding with CO₂, the distorted square pyramidal geometry along with a smaller d-orbital splitting should be only partially recovered owing to the weaker interaction compared to that of H₂O. The lowest energy region of the UV-vis diffuse reflectance spectra (Figure 2) contains the d-d absorption band reflecting this splitting behavior. Therefore energy shifts in this region can be interpreted as an indirect probe of metal coordination changes. Indeed, the observed spectral behavior of **1** upon *in situ* activation and CO₂ adsorption steps (spectral blue shift followed by partial red shift return) is consistent with the aforementioned predicted changes in metal geometry. However, this type of electronic spectroscopy inadequately measures the more subtle changes in local metal coordination environment, such as the interaction between the close lying copper sites that will invariably influence the d-orbital splitting as well. Moreover, the overlap with other nearby absorption bands, namely LMCT bands confounds the assignment and interpretation of spectral changes. Consequently, these diffuse reflectance data are best complemented by a combination of other structurally sensitive spectroscopy measurements to build a more complete picture of the local metal coordination environment associated with the CO₂ adsorption process.

The XAS results reveal both electronic and structural changes of the Cu sites within the framework first upon transformation into the activated form and then upon exposure to CO₂ gas environment. The edge position at 8990 eV, which remains unshifted throughout the experiment, confirms the Cu²⁺ oxidation state of the metal sites. The XANES region contains a very weak pre-edge feature at 8977 eV attributed to the 1s→3d quadrupole allowed transition. The preserved low intensity of this feature indicates that the Cu sites maintain their high centrosymmetry

upon changes in the axial coordination position. The edge feature at 8985 eV, which is weak in the hydrated material but becomes more pronounced upon *in situ* activation, is assigned to a metal localized 1s to 4p transition with “shakedown” contribution arising from a coupled LMCT transition.^{63, 64} This feature is commonly observed in Cu(II) square planar complexes. Polarized XAS studies on oriented single crystals of Cu(II) complexes with geometries ranging from square planar to tetragonal have revealed unambiguously that this transition involves final states with metal 4p_z character, i.e. oriented perpendicular to the equatorial CuL₄ plane.⁶⁵ Consequently, sensitivity to the nature of metal ligation in the axial position is expected. In the absence of axial coordination, this 4p_z orbital can be regarded as σ -nonbonding and therefore highly localized on the metal center. Axial ligation reduces this Cu 4p_z character and the resulting changes in the valence electron shielding account for the decreased intensity of this edge feature. This is consistent with the 1s→4p_z intensity increase observed upon dehydration. When the framework is loaded with CO₂, the edge feature intensity falls to an intermediate level between those observed for the activated and hydrated forms, which indicates that the CO₂ is indeed interacting with the open metal sites but not as strongly as water.

Analysis and fitting of the EXAFS region provides additional structural information of the metal coordination number and distance changes that occur during the activation and CO₂ adsorption processes. As anticipated, the best fit of the hydrated framework EXAFS spectrum yields only minor deviations from the scattering path distances derived from the crystal structure model. The activated framework data set was best fit using a Cu coordination model that lacks the axially ligated oxygen path, indicating the removal of the coordinated water molecules from the Cu sites upon thermal treatment. EXAFS fitting shows that the Cu-O_{carboxylate} bond distances remained relatively constant throughout the dehydration and adsorption processes. Rather, the distance between the pair of copper atoms that comprise the metal paddle wheel nodes of the framework appears to be more sensitive to the presence or absence of axial interaction with both H₂O and CO₂ molecules. The fits reveal a 0.1 Å reduction in Cu-Cu distance upon activation from the hydrated to dehydrated form. This change is consistent with that derived from other EXAFS work on the activation of the well-studied HKUST-1 MOF also with paddlewheel-like nodes.³⁹ Following exposure of the activated framework to CO₂, the fit of the resulting spectrum yields a Cu-Cu distance of 2.63 Å, which is close to the 2.65 Å of the hydrated version. This change implies that CO₂ interaction with the exposed metal sites induces a return to the distorted tetragonal Cu geometry similar to that of H₂O coordination. The large σ^2 values associated with the axial Cu-O paths obtained from the fits of both the hydrated and CO₂-loaded frameworks indicate a higher level of disorder as expected for these labile coordinated molecules in each case. While the EXAFS fitting results point to more subtle structural implications of the activation and CO₂ adsorption processes, the complexity of the structure and the resulting overlapping scattering paths yield a considerably congested EXAFS spectrum. The resulting uncertainties in the fits demand caution against over interpretation and prevents a truly accurate assessment of the coordination distances beyond the first shell.

Raman data collected under identical conditions provides the necessary complementary measure of the local metal structure changes incurred during the activation and CO₂ loading processes. First, the disappearance (and reappearance upon rehydration) of the mode involving the Cu-O_{water} stretch at 496 cm⁻¹ confirms the loss of the coordinated water molecules upon activation. Furthermore, changes in the low frequency region containing the Cu-Cu stretch are consistent with the inter-metallic distances derived from EXAFS fitting described above. Specifically, in the hydrated framework, the broad feature with maximum around 170 cm⁻¹ gives way to a new peak at 230 cm⁻¹ upon *in situ* activation. This peak then red shifts to 223 cm⁻¹ upon CO₂ adsorption. With the dominant vibrational mode contribution to these bands assigned to a mode involving significant Cu-Cu stretch, its behavior provides further evidence that there is increased metal-metal interaction (i.e. stronger force constant for interaction and shorter Cu-Cu distance) first upon removal of axially ligated solvent molecules and then also when loaded with CO₂. Moreover, the frequency shift of this band in the latter case indicates that the weaker Cu-CO₂ interaction causes a smaller perturbation of the Cu-Cu interaction than found in the framework with hydrated Cu sites.

It should be further noted that metal coordination geometry changes upon activation and/or different gas adsorption conditions are well documented for other MOF structures with potentially open metals sites. Notably, Long et al. reported a square planar to tetrahedral geometry change in a Co(II)-(1,4-benzenedipyrozolate) MOF upon the multi-step N₂ adsorption process as revealed by a combination of *in situ* microcalorimetry and UV-vis-NIR diffuse reflectance spectroscopy.⁶⁶ Similarly, we showed an octahedral to tetrahedral geometry change for a flexible Co(II)-based MOF upon activation using *in situ* XAS.⁴¹

2. Linker localized structure changes upon activation and CO₂ adsorption

In this section we discuss structural changes incurred by the triazine linkers within **1** during the activation and CO₂ loading processes. EXAFS is not sensitive to longer range distances from the absorbing Cu sites, so we turn to Raman spectroscopy and the behavior of the linker localized vibrational modes for inferring more structural information about these framework components. Most of these modes, which include distortions of the triazine core, secondary amine and phenyl group, undergo some degree of red-shift in frequency (3-7 cm⁻¹) upon removal of the framework coordinated and encapsulated water molecules as outlined in Table 2. This most likely reflects an overall lower energy and cooperative relaxation that the linker system experiences in the process. The crystal structure of the hydrated framework reveals a slightly twisted orientation of the phenyl rings relative to the triazine core yet by DFT geometry optimization, the H₆TDPAT molecule alone has a planar structure. Therefore, the Raman behavior upon dehydration and in comparison to the H₆TDPAT reference spectrum (Figure S2) indicates a transition to this less strained linker geometry. When CO₂ is introduced to the activated framework, some changes in linker localized mode frequencies are observed but the subtlety of these frequency shifts compared to those involving the metal sites however, indicates that the amine site-CO₂ interaction imparts negligible structural change to the linkers.

3. CO₂ interactions with dually functionalized framework

Evidence of the CO₂ interactions with the different potential binding sites within this dually functionalized framework is provided by the behavior of both the Raman active CO₂ vibrational modes and those of the framework. The characteristic CO₂ Fermi resonance peaks at 1388 and 1285 cm⁻¹ are observed when the framework is exposed to CO₂ gas environment. Their unaltered frequency and sharpness indicates they are attributed to the non-interacting (or very weakly interacting) CO₂ molecules within the vicinity of the laser focus. The new band observed at 1381 cm⁻¹ in this spectrum is attributed to the CO₂ molecules that are coordinated within the framework. A shift to lower frequency of the upper Fermi resonance band is expected upon coordination since the accompanying change in electron density induces symmetry breaking of the linear molecule.⁶⁷ To determine the relative contributions of the linker versus metal site coordination in producing this observed spectral change, these Raman data were compared with that obtained from a sample purged with “wet” CO₂ (ie the activated framework was purged with H₂O saturated CO₂ gas). In this case, H₂O, with its higher affinity for metal binding, will preferentially coordinate the open metal sites,²³ rendering only the secondary amine binding sites on the linker available for CO₂ binding. The spectrum shows only the sharp Fermi dyad peaks and a complete absence of the lower frequency peak around 1381 cm⁻¹. This observation implies that only coordination with the open metal sites strongly perturbs the electronics and symmetry of the CO₂ molecules. This approach of “poisoning” the metal sites to differentiate contributions to gas binding behavior has been successfully applied in other vibrational spectroscopy studies of MOF CO₂ adsorption.⁶⁸ The Raman spectrum of the CO₂/H₂O loaded framework, **I**_{CO₂/H₂O} exposes the interaction between CO₂ and the triazine linkers with the slight out of plane distortion found in the initial hydrated version, **1**. As shown in Figure 4 and outlined in Table 2, all the phenyl localized vibrational modes, such as the breathing mode at 996 cm⁻¹ and C-C stretch mode at 1598 cm⁻¹ shows negligible change after CO₂ adsorption (<1 cm⁻¹). In contrast, the triazine breathing mode at 978 cm⁻¹ and the secondary amine modes involving a C-N stretching and N-H wagging motion at 1277, 1328 and 1441 cm⁻¹ and all experience a red shift of at least 2 cm⁻¹. The red shift of these peaks is consistent with the lowered force constants expected for electron donating interactions with CO₂. Shifts of this magnitude for these modes are not observed however when comparing the spectra of the activated versions, **I**_{act} vs **I**_{CO₂}. This suggests that the amine groups serve as stronger binding sites for CO₂ in the hydrated form, when the out-of-plane distortion of the triazine linker most likely enhances its Lewis basicity. These observations are consistent with the predicted enhanced selectivity of **1** for CO₂ over N₂ in the presence of water vapor compared to the dry binary mixture.²³

Conclusions

In this work, the structural changes and CO₂ binding interactions in an *rht*-type MOF material with multiple potential binding sites were probed by *in situ* UV-vis, XAS and Raman spectroscopy methods. This combined spectroscopic analysis provided molecular level structural details on the reversible square

pyramidal to square planar Cu coordination geometry changes that occur in this MOF upon activation and the partial recovery when CO₂ is coordinated to the metal sites. Both XAS and Raman indicated that the relative strength of Cu-Cu interaction across the paddle wheel nodes was inversely proportional to the strength of ligation in the opposite axial position (i.e. H₂O or CO₂ interaction). EXAFS fitting revealed a contraction of the Cu-Cu distance ~ 0.1 Å upon activation from the hydrated to dehydrated form. The *in situ* Raman studies showed that the dehydration process produced larger structural rearrangements of the framework compared to subsequent CO₂ adsorption. Comparisons between the Raman data collected for the dry and wet CO₂ loaded frameworks provide strong experimental evidence for the separate interactions of CO₂ with the open metal sites and the linker amine/triazine groups. The Raman measurements also revealed new subtle structural changes of the linker upon framework activation that may have important implications for subsequent CO₂ adsorption. These results support the concept that Lewis base functionalized linkers provide binding sites for CO₂ in addition to the open metal coordination sites, as predicted computationally,^{22, 23} but indicate that the linker distortion that occurs upon activation can influence the effectiveness of the binding interaction possibly by altering its basicity.

Acknowledgements

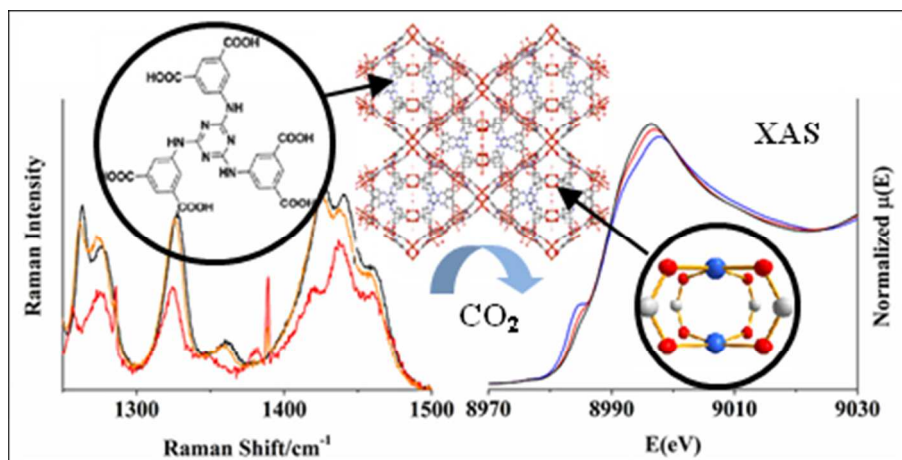
Use of the National Synchrotron Light Source, Brookhaven National Laboratory, was supported by the U.S. Department of Energy, Office of Science, Office of Basic Energy Sciences, under Contract No. DE-AC02-98CH10886. We thank Dr. Stephen Ehrich and Dr. Nbrojsa Marinkovic at NSLS for their help during XAS experiments. JVL acknowledges the donors of the American Chemical Society Petroleum Research Fund for partial support of this research (Grant #52148-DN15). HW and JL would like to acknowledge the partial support by the U.S. Department of Energy (DOE Grant No. DE-FG02-08ER46491) for the sample synthesis and structure characterization involved in this work.

Notes and references

- ^a Department of Chemistry, Rutgers University, Newark, New Jersey 07102, United States E-mail: jlockard@rutgers.edu
^b Department of Chemistry and Chemical Biology, Rutgers University-New Brunswick, Piscataway, New Jersey 08854, United States
 † Electronic Supplementary Information (ESI) available: synthesis details, PXRD characterization, experimental and theoretical Raman spectra of reference systems, and DFT computational details. See DOI: 10.1039/b000000x/
- 1 H. Furukawa, K. E. Cordova, M. O’Keeffe and O. M. Yaghi, *Science*, 2013, **341**,
 - 2 C. Wang, D. Liu and W. Lin, *J Am Chem Soc*, 2013, **135**, 13222-13234.
 - 3 M. L. Foo, R. Matsuda and S. Kitagawa, *Chem. Mater.*, 2014, **26**, 310-322.
 - 4 J. Lee, O. K. Farha, J. Roberts, K. A. Scheidt, S. T. Nguyen and J. T. Hupp, *Chem Soc Rev*, 2009, **38**, 1450-1459.
 - 5 J. Liu, P. K. Thallapally, B. P. McGrail, D. R. Brown and J. Liu, *Chem*

- Soc Rev*, 2012, **41**, 2308-2322.
- 6 K. Sumida, D. L. Rogow, J. A. Mason, T. M. McDonald, E. D. Bloch, Z. R. Herm, T.-H. Bae and J. R. Long, *Chem. Rev.*, 2012, **112**, 724-781.
- 7 H. Wu, Q. Gong, D. H. Olson and J. Li, *Chem. Rev.*, 2012, **112**, 836-868.
- 8 Y. Cui, Y. Yue, G. Qian and B. Chen, *Chem. Rev.*, 2012, **112**, 1126.
- 9 Z. Hu, B. J. Deibert and J. Li, *Chem Soc Rev*, 2014, **43**, 5815-5840.
- 10 N. L. Rosi, J. Kim, M. Eddaoudi, B. Chen, M. O'Keeffe and O. M. Yaghi, *J Am Chem Soc*, 2005, **127**, 1504-1518.
- 11 P. D. C. Dietzel, Y. Morita, R. Blom and H. Fjellvåg, *Angew. Chem. Int. Ed.*, 2005, **44**, 6354-6358.
- 12 P. D. C. Dietzel, R. E. Johnsen, H. Fjellvåg, S. Bordiga, E. Groppo, S. Chavan and R. Blom, *Chem Comm*, 2008, 5125-5127.
- 13 S. R. Caskey, A. G. Wong-Foy and A. J. Matzger, *J Am Chem Soc*, 2008, **130**, 10870-10871.
- 14 D. Britt, H. Furukawa, B. Wang, T. G. Glover and O. M. Yaghi, *P Natl Acad Sci*, 2009, **106**, 20637-20640.
- 15 S. Couck, J. F. M. Denayer, G. V. Baron, T. Rémy, J. Gascon and F. Kapteijn, *J Am Chem Soc*, 2009, **131**, 6326-6327.
- 16 J. An, S. J. Geib and N. L. Rosi, *J Am Chem Soc*, 2009, **132**, 38-39.
- 17 H. Xu, Y. He, Z. Zhang, S. Xiang, J. Cai, Y. Cui, Y. Yang, G. Qian and B. Chen, *Journal of Materials Chemistry A*, 2013, **1**, 77-81.
- 18 X. Rao, J. Cai, J. Yu, Y. He, C. Wu, W. Zhou, T. Yildirim, B. Chen and G. Qian, *Chem Comm*, 2013, **49**, 6719-6721.
- 19 N. Nijem, P. Canepa, L. Kong, H. Wu, J. Li, T. Thonhauser and Y. J. Chabal, *J. Phys.: Condens. Matter*, 2012, **24**, 424203.
- 20 L.-C. Lin, J. Kim, X. Kong, E. Scott, T. M. McDonald, J. R. Long, J. A. Reimer and B. Smit, *Angew. Chem. Int. Ed.*, 2013, **52**, 4410-4413.
- 21 N. Planas, A. L. Dzubak, R. Poloni, L.-C. Lin, A. McManus, T. M. McDonald, J. B. Neaton, J. R. Long, B. Smit and L. Gagliardi, *J Am Chem Soc*, 2013, **135**, 7402-7405.
- 22 T. Pham, K. A. Forrest, J. Eckert, P. A. Georgiev, A. Mullen, R. Luebke, A. J. Cairns, Y. Belmabkhout, J. F. Eubank, K. McLaughlin, W. Lohstroh, M. Eddaoudi and B. Space, *J Phys Chem C*, 2014, **118**, 439-456.
- 23 Z. Zhang, Z. Li and J. Li, *Langmuir*, 2012, **28**, 12122-12133.
- 24 B. Li, Z. Zhang, Y. Li, K. Yao, Y. Zhu, Z. Deng, F. Yang, X. Zhou, G. Li, H. Wu, N. Nijem, Y. J. Chabal, Z. Lai, Y. Han, Z. Shi, S. Feng and J. Li, *Angew. Chem. Int. Ed.*, 2012, **51**, 1412-1415.
- 25 R. Luebke, J. F. Eubank, A. J. Cairns, Y. Belmabkhout, L. Wojtas and M. Eddaoudi, *Chem Comm*, 2012, **48**, 1455-1457.
- 26 D. Zhao, D. Yuan, D. Sun and H.-C. Zhou, *J Am Chem Soc*, 2009, **131**, 9186-9188.
- 27 J. F. Eubank, F. Nouar, R. Luebke, A. J. Cairns, L. Wojtas, M. Alkordi, T. Bousquet, M. R. Hight, J. Eckert, J. P. Embs, P. A. Georgiev and M. Eddaoudi, *Angew. Chem. Int. Ed.*, 2012, **51**, 10099-10103.
- 28 O. K. Farha, A. Özgür Yazaydin, I. Eryazici, C. D. Malliakas, B. G. Hauser, M. G. Kanatzidis, S. T. Nguyen, R. Q. Snurr and J. T. Hupp, *Nat Chem*, 2010, **2**, 944-948.
- 29 F. Nouar, J. F. Eubank, T. Bousquet, L. Wojtas, M. J. Zaworotko and M. Eddaoudi, *J Am Chem Soc*, 2008, **130**, 1833-1835.
- 30 B. Zheng, J. Bai, J. Duan, L. Wojtas and M. J. Zaworotko, *J Am Chem Soc*, 2011, **133**, 748-751.
- 31 Y. Yan, S. Yang, A. J. Blake, W. Lewis, E. Poirier, S. A. Barnett, N. R. Champness and M. Schroder, *Chem Comm*, 2011, **47**, 9995-9997.
- 32 Y. Yan, M. Suyetin, E. Bichoutskaia, A. J. Blake, D. R. Allan, S. A. Barnett and M. Schroder, *Chem Sci*, 2013, **4**, 1731-1736.
- 33 G. Agostini, C. Lamberti, L. Palin, M. Milanesio, N. Danilina, B. Xu, M. Janousch and J. A. van Bokhoven, *J Am Chem Soc*, 2009, **132**, 667-678.
- 34 D. E. Doronkin, M. Casapu, T. Günter, O. Müller, R. Frahm and J.-D. Grunwaldt, *J Phys Chem C*, 2014, **118**, 10204-10212.
- 35 D. Grandjean, A. M. Beale, A. V. Petukhov and B. M. Weckhuysen, *J Am Chem Soc*, 2005, **127**, 14454-14465.
- 36 I. J. Drake, Y. Zhang, M. K. Gilles, C. N. Teris Liu, P. Nachimuthu, R. C. C. Perera, H. Wakita and A. T. Bell, *J Phys Chem B*, 2006, **110**, 11665-11676.
- 37 G. Plazenet, E. Payen, J. Lynch and B. Rebours, *J Phys Chem B*, 2002, **106**, 7013-7028.
- 38 S. Bordiga, F. Bonino, K. P. Lillerud and C. Lamberti, *Chem Soc Rev*, 2010, **39**, 4885-4927.
- 39 C. Prestipino, L. Regli, J. G. Vitillo, F. Bonino, A. Damin, C. Lamberti, A. Zecchina, P. L. Solari, K. O. Kongshaug and S. Bordiga, *Chem. Mater.*, 2006, **18**, 1337-1346.
- 40 F. Bonino, S. Chavan, J. G. Vitillo, E. Groppo, G. Agostini, C. Lamberti, P. D. C. Dietzel, C. Prestipino and S. Bordiga, *Chem. Mater.*, 2008, **20**, 4957-4968.
- 41 Y. Chen, J. Zhang, J. Li and J. V. Lockard, *J Phys Chem C*, 2013, **117**, 20068-20077.
- 42 W. S. Drisdell, R. Poloni, T. M. McDonald, J. R. Long, B. Smit, J. B. Neaton, D. Prendergast and J. B. Kortright, *J Am Chem Soc*, 2013, **135**, 18183-18190.
- 43 S. Chavan, J. G. Vitillo, E. Groppo, F. Bonino, C. Lamberti, P. D. C. Dietzel and S. Bordiga, *J Phys Chem C*, 2009, **113**, 3292-3299.
- 44 N. Nijem, P. Thissen, Y. Yao, R. C. Longo, K. Roodenko, H. Wu, Y. Zhao, K. Cho, J. Li, D. C. Langreth and Y. J. Chabal, *J Am Chem Soc*, 2011, **133**, 12849-12857.
- 45 J. Seo, C. Bonneau, R. Matsuda, M. Takata and S. Kitagawa, *J Am Chem Soc*, 2011, **133**, 9005-9013.
- 46 S. Chavan, J. G. Vitillo, C. Larabi, E. Alessandra Quadrelli, P. D. C. Dietzel and S. Bordiga, *Micropor Mesopor Mat*, 2012, **157**, 56-61.
- 47 N. Nijem, H. Wu, P. Canepa, A. Marti, K. J. Balkus, T. Thonhauser, J. Li and Y. J. Chabal, *J Am Chem Soc*, 2012, **134**, 15201-15204.
- 48 K. Tan, N. Nijem, P. Canepa, Q. Gong, J. Li, T. Thonhauser and Y. J. Chabal, *Chem. Mater.*, 2012,
- 49 Y. Yao, N. Nijem, J. Li, Y. J. Chabal, D. C. Langreth and T. Thonhauser, *Phys Rev B*, 2012, **85**, 064302.
- 50 H. Liu, Y. Zhao, Z. Zhang, N. Nijem, Y. J. Chabal, X. Peng, H. Zeng and J. Li, *Chem. Asian J.*, 2013, **8**, 778-785.
- 51 M. I. Breeze, G. Clet, B. C. Campo, A. Vimont, M. Daturi, J.-M. Grenèche, A. J. Dent, F. Millange and R. I. Walton, *Inorg Chem*, 2013, **52**, 8171-8182.
- 52 L. Hamon, P. L. Llewellyn, T. Devic, A. Ghoufi, G. Clet, V. Guillermin, G. D. Pirngruber, G. Maurin, C. Serre, G. Driver, W. v. Beek, E. Jolimaître, A. Vimont, M. Daturi and G. Férey, *J Am Chem Soc*, 2009, **131**, 17490-17499.
- 53 H. Leclerc, T. Devic, S. Devautour-Vinot, P. Bazin, N. Audebrand, G. Férey, M. Daturi, A. Vimont and G. Clet, *J Phys Chem C*, 2011, **115**, 19828-19840.
- 54 P. J. Chupas, M. F. Ciruolo, J. C. Hanson and C. P. Grey, *J Am Chem Soc*, 2001, **123**, 1694-1702.
- 55 B. Ravel and M. Newville, *J. Synch. Rad.*, 2005, **12**, 537-541.

- 56 J. J. Rehr and R. C. Albers, *Rev Mod Phys*, 2000, **72**, 621-654.
- 57 K. Nakamoto, *Infrared and Raman Spectra of Inorganic and Coordination Compounds, Part B*. 6th ed., John Wiley & Sons, Inc, 2009
- 58 P. J. Larkin, M. P. Makowski and N. B. Colthup, *Spectro. Chim. Acta A*, 1999, **55**, 1011-1020.
- 59 W. Sawodny, K. Niedenzu and J. W. Dawson, *The Journal of Chemical Physics*, 1966, **45**, 3155-3156.
- 60 G. Socrates, *Infrared and Raman Characteristic Group Frequencies*. 3rd ed., John Wiley & Sons, Ltd, 2001
- 61 M. K. Marchewka, *Bull. Korean Chem. Soc.*, 2004, **25**, 466-470.
- 62 D. L. Phillips, C.-M. Che, K. H. Leung, Z. Mao and M.-C. Tse, *Coordin Chem Rev*, 2005, **249**, 1476-1490.
- 63 S. E. Shadle, J. E. Penner-Hahn, H. J. Schugar, B. Hedman, K. O. Hodgson and E. I. Solomon, *J Am Chem Soc*, 1993, **115**, 767-776.
- 64 L. S. Kau, D. J. Spira-Solomon, J. E. Penner-Hahn, K. O. Hodgson and E. I. Solomon, *J Am Chem Soc*, 1987, **109**, 6433-6442.
- 65 T. A. Smith, J. E. Penner-Hahn, M. A. Berding, S. Doniach and K. O. Hodgson, *J Am Chem Soc*, 1985, **107**, 5945-5955.
- 66 F. Salles, G. Maurin, C. Serre, P. L. Llewellyn, C. Knöfel, H. J. Choi, Y. Filinchuk, L. Oliviero, A. Vimont, J. R. Long and G. r. Férey, *J Am Chem Soc*, 2010, **132**, 13782-13788.
- 67 H. Forster and M. Schumann, *Journal of the Chemical Society, Faraday Transactions 1: Physical Chemistry in Condensed Phases*, 1989, **85**, 1149-1158.
- 68 P. L. Llewellyn, S. Bourrelly, C. Serre, A. Vimont, M. Daturi, L. Hamon, G. De Weireld, J.-S. Chang, D.-Y. Hong, Y. Kyu Hwang, S. Hwa Jhung and G. Férey, *Langmuir*, 2008, **24**, 7245-7250.



76x38mm (150 x 150 DPI)